Petroleum Science 22 (2025) 3817–3829

Contents lists available at ScienceDirect

Petroleum Science

journal homepage: www.keaipublishing.com/en/journals/petroleum-science

Original Paper

Hydrate formation and agglomeration in Pickering emulsions stabilized by hydrophilic and hydrophobic nano-$CaCO_3$ particles

Dong-Dong Guo [a,b], Wen-Jia Ou [b], Yun-Hong Zhang [a], Heng-Yin Zhu [a], Shahab Ud Din [c], Ren Wang [d], Fu-Long Ning [b,*]

[a] The Innovation Base of Fine Mine Prospecting and Intelligent Monitoring Technology, School of Earth and Environment, Anhui University of Science and Technology, Huainan, 232001, Anhui, China
[b] Engineering Research Center of Rock-Soil Drilling & Excavation and Protection, Ministry of Education, China University of Geosciences, Wuhan, 430074, Hubei, China
[c] Department of Oil-Gas Field Development, College of Petroleum Engineering, China University of Petroleum (Beijing), Beijing, 102249, China
[d] CNPC Engineering Technology Research and Development Company Limited, Beijing, 102206, China

ARTICLE INFO

Article history:
Received 24 October 2024
Received in revised form
4 May 2025
Accepted 14 August 2025
Available online 21 August 2025

Edited by Min Li

Keywords:
Gas hydrate
Pickering emulsion
Nano-$CaCO_3$ particles
Hydrophilicity and hydrophobicity
Inhibition effect

ABSTRACT

The stability of oil-dominated emulsions, including oil-based drilling fluids and crude oils, is crucial for mitigating gas hydrate risks in the petroleum and natural gas industries. Nanoparticles can stabilize oil-water systems (Pickering emulsions) by residing at the oil-water interface. However, their effects on the kinetics of hydrate formation in these systems remain unclear. To address this, we experimentally investigated how hydrophilic and hydrophobic nano-$CaCO_3$ influence CH_4 hydrate formation within dynamic oil-water systems. A series of hydrate formation experiments were conducted with varying water cuts and different concentrations of nano-$CaCO_3$ at a particle size of 20 nm, under 3 °C and 6 MPa. The induction time, hydrate formation volume, and hydrate growth rate were measured and calculated. The results indicate that hydrophilic nano-$CaCO_3$ generally inhibits hydrate formation, particularly at high water cuts, while hydrophobic nano-$CaCO_3$ can significantly inhibit or even prevent hydrate formation at low water cuts. Water cut strongly influences the kinetics of hydrate formation, and nanoparticle concentration also impacts the results, likely due to changes in oil-water interface stability caused by nanoparticle distribution. This study will offer valuable insights for designing deepwater oil-based drilling fluids using nanoparticles and ensuring safe multiphase flow in deepwater oil and gas operations.

1. Introduction

Natural gas hydrates are nonstoichiometric inclusion compounds created when water molecules combine with natural gas under conditions of low temperature and high pressure (Sloan, 2003). They are commonly found in petrochemical pipelines and extreme environments like submarine sediments, polar regions, and even on other planets (Chastain and Chevrier, 2007; Chong et al., 2016; Hammerschmidt, 1934; Makogon, 2010). Beyond their energy potential and environmental significance, gas hydrates have promising applications in gas storage and transport (Veluswamy et al., 2017), CO_2 capture (Ma et al., 2016; Ndlovu et al., 2024), desalination (Lim et al., 2023; Park et al., 2011), air conditioning (Park et al., 2023), and ion separation (Seo et al., 2024). Despite these advantages, gas hydrates pose a significant risk to offshore oil and gas operations, particularly as water depths increase. The low-temperature, high-pressure conditions in deepwater drilling promote hydrate formation, which can lead to blockages in pipelines, annular spaces, or blowout preventers, disrupting drilling activities (Kar et al., 2016; Sloan and Koh, 2008). Oil-based drilling fluids (OBDF) and synthetic-based fluids, both classified as oil-water (OW) emulsions, are commonly used in these environments due to their strong inhibitory properties, high temperature resistance, and reservoir protection (Mikhienkova et al., 2022; Ning et al., 2011; Smith et al., 2014). However, hydrate formation and agglomeration can negatively impact the

* Corresponding author.
E-mail address: nflzx@cug.edu.cn (F.-L. Ning).
Peer review under the responsibility of China University of Petroleum (Beijing).

https://doi.org/10.1016/j.petsci.2025.08.022

stability and performance of these emulsions, creating additional challenges for deepwater drilling.

Although completely avoiding hydrate formation in pipelines is challenging, researchers have proposed a solution: allowing hydrates to form but keeping them under control. Chemical inhibitors like anti-agglomerants (AAs) are often used to ensure flow in pipelines (Aman et al., 2010; Aman and Koh, 2016; Ning et al., 2022; Wang et al., 2023). However, these additives raise concerns about cost and environmental impact. Recently, particle-stabilized emulsions (Pickering emulsions) have attracted attention due to their environmental benefits and reduced reliance on harmful surfactants (Ortiz et al., 2020; Wu and Ma, 2016; Zhao et al., 2022). Emulsion stability is a key factor in hydrate agglomeration under both static and flowing conditions (Guo et al., 2020; Lachance et al., 2008). Studies have shown that Pickering emulsions, formed by nanoparticle adsorption at specific temperatures and pressures, outperform traditional surfactant-stabilized emulsions in pipeline applications (Ahuja et al., 2018; Chevalier and Bolzinger, 2013; Zhang et al., 2022). For instance, Raman et al. (2016) found that emulsions with moderately hydrophobic solid particles maintain stability after hydrate formation and dissociation.

Nanoparticles have been increasingly applied to prevent hydrate-induced blockages (Baek et al., 2015; Cha et al., 2014; Ma et al., 2016; Zhang et al., 2022). Hydrophobic silica nanoparticles, for example, can form a particle layer at the oil-water interface, limiting the contact area where hydrates form (Cha et al., 2014). This phenomenon has been replicated in systems using propane-cyclopentane-water with activated carbon, where the particle layer restricts both hydrate crystallization and further growth by covering the oil-water interface (Baek et al., 2015). Similarly, nanoparticle layers can delay or prevent adhesion of hydrate probes, offering greater anti-adhesion force compared to traditional surfactants like Span 20 (Ma et al., 2016). Moreover, nanoparticles significantly influence hydrate formation kinetics in OW systems (Ahuja, 2015, Ahuja et al., 2018; Baek et al., 2015; Cha et al., 2014; Song et al., 2020). Song et al. (2020) reported that cellulose nanocrystals prolong hydrate induction time and increase residual pressure. Hydrophobic nanoparticles at the OW interface can also inhibit gas and liquid molecule migration, delaying hydrate nucleation and growth (Ahuja, 2015; 2018; Baek et al., 2015; Cha et al., 2014). Interestingly, low concentrations of hydrophobic silica nanoparticles act as hydrate inhibitors in water-in-oil emulsions, but at higher concentrations (above 0.5 wt%), the formation rate increases (Baek et al., 2019). In addition, some studies have also considered the recovery of nanoparticles to avoid adverse effects caused by particle deposition, such as using recyclable magnetic nanoparticles as hydrate inhibitors and anti-agglomerants (Min et al., 2020). While many studies demonstrate the inhibition effect of nanoparticles in OW systems, other research suggests that hydrophobic particles may promote hydrate formation in bulk water systems by adsorbing gas molecules and orienting water molecules to form hydrate cages (Aliabadi et al., 2015; Deng et al., 2023; Farhang et al., 2014; Guo et al., 2022; Park et al., 2012; Wang et al., 2019; Wei and Maeda, 2023; Zhou et al., 2014).

Studies have shown that nanoparticles distributed at the OW interface can enhance emulsion stability, thereby inhibiting hydrate agglomeration in OW systems. However, in pure water systems, nanoparticles often accelerate hydrate formation. The effects of nanoparticles on hydrate formation kinetics in OW systems remain unclear, and the role of nanoparticle surface wettability has not been fully understood. Surface wettability is crucial as it influences the type of OW emulsion, which in turn affects the anti-agglomeration behavior of hydrates (Zhang et al., 2022). To address this gap, this study explores the impact of hydrophilic and hydrophobic nano-$CaCO_3$ particles (20 nm) on hydrate nucleation, growth kinetics, and aggregation in OW systems with varying water cuts (10%–50%, considering both oil-based drilling fluids and crude oil conditions). The choice of nano-$CaCO_3$ as the solid emulsifier in this study is driven by considerations of environmental protection and reservoir preservation. Nano-$CaCO_3$ is non-toxic, ensuring it will not harm marine or permafrost environments. Additionally, compared to nano-SiO_2, nano-$CaCO_3$ is more easily decomposed and treated, making it a better option for preserving reservoir permeability (Guo et al., 2022). Experiments were conducted at 3 °C and 6 MPa to measure induction time, hydrate formation amount, and average formation rate. Comparative analyses were performed to evaluate the effects of nanoparticle wettability on hydrate behavior. This research will provide valuable insights into the mechanisms behind nanoparticle-induced anti-agglomeration and inhibition effects, with implications for their application in deep-water oil and gas drilling and multiphase flow transport.

2. Experimental section

2.1. Materials

The CH_4 gas (99.9% purity) used in this study was supplied by Wuhan Niuruide Trading Co., Ltd. Hydrophilic and hydrophobic $CaCO_3$ nanoparticles (20 nm) were obtained from American Specialty Minerals Inc. The reason for selecting 20 nm $CaCO_3$ is that in pure water systems, both hydrophilic and hydrophobic nanoparticles exhibited the best inhibitory or promoting effects at a particle size of 20 nm, compared to 70 and 700 nm (Guo et al., 2022). The hydrophilic $CaCO_3$ nanoparticles were produced via sedimentation, while the hydrophobic particles were derived by coating the hydrophilic ones with a coupling agent. These nanoparticles are irregularly shaped and prone to forming agglomerates. Full characterization including scanning electron microscopy (SEM) images of the nano-$CaCO_3$ particles can be found in our previous work (Guo et al., 2022). Ultra-pure water (UPW) with a resistivity greater than 18.25 MΩ cm was prepared using a UPW-S Millipore unit. The mineral oil, supplied by Dongguan Lubricating Oil Ltd., consists mainly of *n*-alkanes (C_{14}–C_{18}), as analyzed using gas chromatography-mass spectrometry (GC/MS, Agilent 7890A/5975C, USA) (Guo et al., 2020).

2.2. Experimental apparatus

The experimental setup for hydrate formation is illustrated in Fig. 1, which was previously used in our studies (Guo et al., 2022; Wang et al., 2019). The system consists of a cylindrical stainless-steel autoclave (50 mm internal diameter, 330 mm height, ~650 mL volume) immersed in a temperature-controlled water bath. The autoclave has two opposing Pyrex-glass windows (30 mm diameter) at mid-height. A gas supply line, equipped with a pressure regulator, connects the autoclave to a high-pressure methane cylinder. Temperature sensors placed at the top and bottom of the autoclave monitor the liquid and gas phases, respectively, while a pressure sensor with ±5 kPa accuracy records pressure data. Sensor readings are captured every 2 s by a data acquisition system for further analysis.

2.3. Experimental procedure

In this study, the constant volume method was employed, where the system remains closed, and pressure drop in the autoclave indicates gas hydrate formation (Abay and Svartaas, 2010;

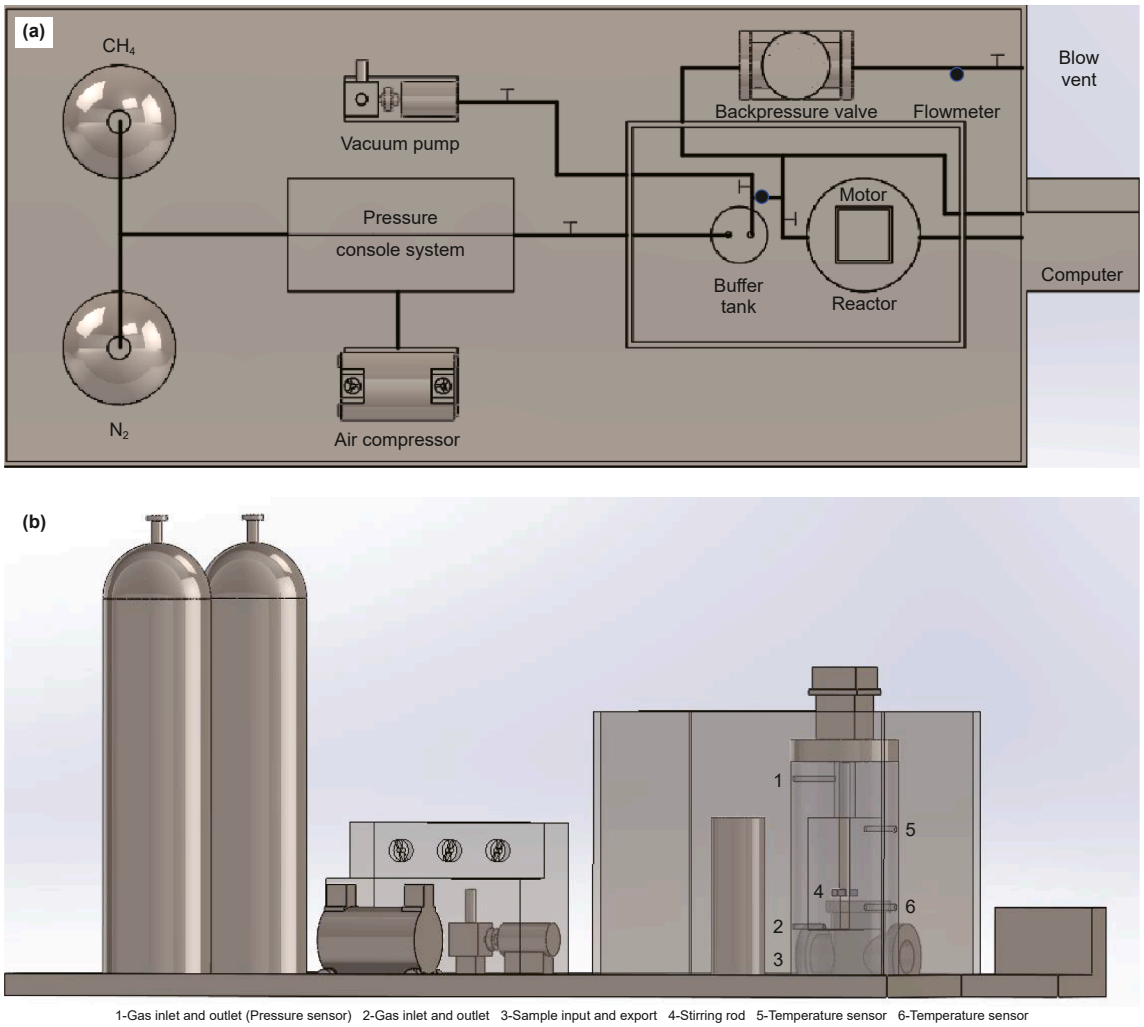

Fig. 1. Schematic representation of the experimental setup for hydrate formation in OW systems with varying water cuts and nanoparticle concentrations: **(a)** vertical view of the setup; **(b)** front view of the setup.

Guo et al., 2022; Sloan and Koh, 2008; Zhang et al., 2007). This approach was used to investigate the effects of nanoparticle wettability and concentration on the kinetics of CH_4 hydrate formation in OW systems.

The experimental procedures are as follows: (1) Thoroughly clean the apparatus several times with UPW + detergent, followed by rinsing with UPW; (2) Inject 99.9% pure N_2 into the pressure autoclave to test the seal, then use a vacuum pump to remove as much N_2 as possible; (3) Prepare OW systems with varying water cuts and nanoparticle concentrations (0.1, 0.5, 1.0, 2.0 wt%) using a high-speed blender set at 20,000 rpm. Hydrophilic nanoparticles are first mixed with water, followed by the oil phase (water and oil volumes are calculated based on the water cut; hydrophilic nano-$CaCO_3$ is added to the water phase and stirred for 30 s, then mixed with oil and stirred three times for 30 s each). Hydrophobic nanoparticles are first mixed with the oil, then combined with the water phase (hydrophobic nano-$CaCO_3$ is stirred into the oil for 30 s, followed by the addition of UPW, stirred three times for 30 s each); (4) Observe the formation of the emulsion and its size distribution using an optical microscope; (5) Introduce approximately 300 mL of the prepared fluid or UPW into the autoclave under vacuum, then close the valve and apply vacuum again for at least 10 min; (6) Pressurize the buffer vessel to 10.0 MPa with CH_4, and maintain both the buffer vessel and autoclave at 3 °C in a water bath to expedite hydrate formation and reduce induction time. Stir the fluid in the autoclave at 800 rpm to enhance cooling and prevent nanoparticle aggregation. (7) Once the system temperature stabilizes at 3 °C, close the stirrer and open the gas inlet valve to pressurize the autoclave with CH_4 from the buffer vessel until reaching 6.0 MPa (the phase-equilibrium pressure P_{eq} at 3 °C is 3.49 MPa, with a driving force of 2.51 MPa). Then, close the valve and stir at 800 rpm to accelerate hydrate formation; (8) Begin recording temperature and pressure data every 2 s using a data acquisition system, marking this as time zero for the experiment.

2.4. Data processing for kinetics of the hydrate formation

The temperature and pressure curves over time during hydrate formation in OW systems, both with and without nanoparticles, were obtained to visually represent the changes in the autoclave during the experiment (Guo et al., 2022). For instance, Fig. 2 shows the profiles of temperature and pressure during hydrate formation in a 30% OW system containing 0.5 wt% hydrophobic nano-$CaCO_3$. A sudden change in pressure and temperature, referred to as the "sudden pressure drop" and "temperature increase" indicates the onset of large-scale hydrate formation. When the pressure stabilizes and no longer decreases, it signifies that the hydrate formation process is nearing completion. This time is recorded as the end

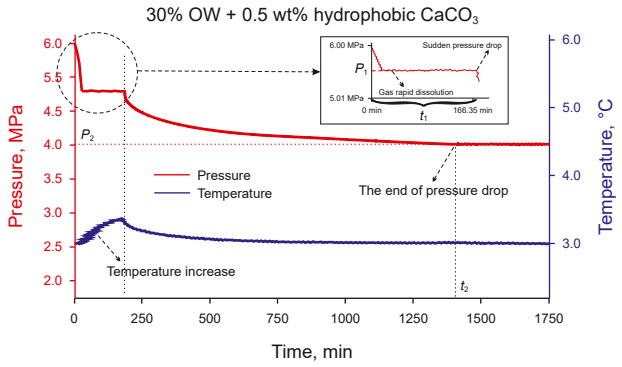

Fig. 2. The temperature and pressure variations during hydrate formation in a 30% OW system with 0.5 wt% hydrophobic $CaCO_3$ nanoparticles are presented under the initial experimental conditions of 3 °C and 6 MPa. The onset of hydrate formation is marked by a sudden pressure drop (P_1) and a corresponding rise in temperature, which indicates the start time (t_1). When the pressure stabilizes with no further significant drop (P_2), it indicates that hydrate formation is complete, and the time (t_2) is recorded as the end time of the process.

of hydrate formation. Each experiment was repeated three times to minimize errors, and the average results are presented.

The induction time of hydrate formation is a critical parameter for evaluating the inhibition or acceleration of hydrate crystallization (Guo et al., 2022; Natarajan et al., 1994). Since the formation of a critical-sized hydrate nucleus cannot be directly observed at the macroscopic level (Kashchiev and Firoozabadi, 2003), this study defines the apparent induction time as the period between the complete dissolution of CH_4 and the onset of the sudden pressure drop, as shown in Fig. 2.

Methane consumption is another critical indicator for assessing the inhibition or promotion of hydrate formation (Guo et al., 2022; Park et al., 2012). The quantity of gas consumed during hydrate formation can be determined from the pressure and temperature data using the real gas equation of state (Kakati et al., 2016; Park et al., 2012):

$$\Delta n = n_1 - n_2 = \left(\frac{P_1 V_1}{Z_1} - \frac{P_2 V_2}{Z_2}\right) \times \frac{1}{RT} \tag{1}$$

where, n_1 and n_2 are the initial and final amount of CH_4 consumed, mol; Δn represents the amount of CH_4 consumed, mol; P_1 and P_2 are the initial and final pressures, MPa, respectively, after complete CH_4 dissolution and after hydrate formation has ceased; R is the universal gas constant, 8.31441 J·mol^{-1}·K^{-1}; T is the CH_4 temperature, K; V_1 and V_2 are the initial and final volumes of CH_4, m^3, with V_1 approximately 400 mL and V_2 about 370 mL (the total volume of the autoclave is 650 mL, containing 250 mL of liquid; during hydrate formation, fluid volume expands by approximately 12% under the experimental conditions (Guo et al., 2022)); Z_1, Z_2 represent the initial and final compressibility factors, respectively. The compressibility factor (Z) is calculated using the following equation (Ahmed, 1989; Sloan and Koh, 2008):

$$Z = 1 + \left(A_1 + \frac{A_2}{T_{pr}} + \frac{A_3}{T_{pr}^3}\right) + \left(A_4 + \frac{A_5}{T_{pr}}\right)\rho_r^2 + \left(\frac{A_5 A_6}{T_{pr}}\right)\rho_r^5 - \frac{A_7}{T_{pr}^3}\rho_r^2\left(1 + A_8\rho_r^2\right)\exp\left(-A_8\rho_r^2\right) \tag{2}$$

where A_i is given parameters ($A_1 = 0.31506237$, $A_2 = -1.0467099$, $A_3 = -0.57832729$, $A_4 = 0.53530771$, $A_5 = -0.61232032$, $A_6 = -0.10488813$, $A_7 = 0.68157001$, $A_8 = 0.68446549$); P_{pr} is comparative pressure; T_{pr} is comparative temperature; ρ_r is methane comparative density. P_{pr}, T_{pr} and ρ_r are calculated as follows:

$$P_{pr} = \frac{P}{P_c}, T_{pr} = \frac{T}{T_c}, \rho_r = 0.27\left(\frac{P_{pr}}{ZT_{pr}}\right) \tag{3}$$

where, P is the pressure of CH_4, MPa; P_c is the critical pressure of CH_4, about 4.60 MPa (Ahmed, 1989; Sloan and Koh, 2008); T is the temperature of CH_4, K; T_c is the critical temperature of CH_4 gas, about 191.11 K (Ahmed, 1989; Sloan and Koh, 2008). Thus, the consumption of CH_4 can be calculated by substituting the experimental data into Eqs. (1)–(3).

The rate of hydrate formation is closely linked to the amount of gas consumed during the experimental process (Guo et al., 2022; Park et al., 2012). This parameter offers valuable insights into the kinetics of continuously growing hydrate crystals. In this study, the hydrate formation rate is expressed as the average CH_4 consumption rate, calculated from the end of the induction time to the conclusion of the formation process. The hydrate formation rate can be derived using the following equation (Guo et al., 2022; Park et al., 2012):

$$v = \frac{\Delta n}{(t_2 - t_1)} \tag{4}$$

where, v represents the average CH_4 consumption rate, mol/min; t_2 denotes the end time of hydrate formation, min; t_1 accounts for the sum of the induction time and the time taken for CH_4 dissolution, min. A lower formation rate is preferred to enhance the safety of the hydrate drilling process. The detailed calculation procedure can be found in our previous studies (Guo et al., 2022; Wang et al., 2019).

3. Results

Using the experimental data acquisition method described above, we obtained data on CH_4 hydrate formation across various water cuts in OW systems with different concentrations of hydrophilic and hydrophobic nano-$CaCO_3$ particles (see Tables 1 and 2). Table 1 summarizes the kinetic parameters for hydrate formation in OW systems containing hydrophilic nano-$CaCO_3$, while Table 2 presents the experimental results regarding the impact of hydrophobic nano-$CaCO_3$ particles on hydrate formation.

In this study, alongside the pressure and temperature change curves for hydrate formation in various OW systems, the experimental phenomena within the reactor were monitored and recorded via video. This visual documentation highlights the influence of nanoparticles on hydrate formation and agglomeration, providing valuable support for analyzing hydrate kinetic parameters. Figs. 3 and 4 illustrate the effects of hydrophilic and hydrophobic nanoparticles (at concentrations of 0.1, 0.5, 1.0, and 2.0 wt%) on hydrate formation and agglomeration across different water cuts (10%–50%). Although the images captured are not entirely clear due to the presence of the oil phase and the immersion of the visualization window in the water bath, they still offer some information to explain and analyze the influence of hydrophilic and hydrophobic nanoparticles on hydrate formation and agglomeration.

4. Discussion

4.1. Induction time

A comprehensive evaluation of the effects of hydrophilic and hydrophobic nano-$CaCO_3$ on CH_4 hydrate formation in OW

Table 1
The data on hydrate formation kinetics in various water cuts of OW systems, both with and without hydrophilic nano-$CaCO_3$, were recorded at 3 °C and 6 MPa. The standard deviation is used to represent the uncertainty of data.

Water cut, %	Concentration, wt%	t_1, min	t_2, min	P_1, MPa	P_2, MPa	With/without hydrate
10	0.0	0.00 ± 0.00	84.22 ± 3.01	6.000 ± 0.004	4.752 ± 0.012	with
	0.1	67.49 ± 23.25	1304.05 ± 333.90	4.826 ± 0.110	4.734 ± 0.570	with
	0.5	0.00 ± 0.00	104.26 ± 11.45	6.004 ± 0.004	4.821 ± 0.016	with (very few)
	1.0	0.00 ± 0.00	87.48 ± 1.07	6.006 ± 0.003	4.863 ± 0.001	with (very few)
	2.0	0.00 ± 0.00	81.57 ± 1.24	6.006 ± 0.002	4.865 ± 0.003	with (very few)
20	0.0	179.72 ± 25.26	233.45 ± 49.98	4.894 ± 0.048	4.806 ± 0.047	with
	0.1	128.45 ± 42.69	199.42 ± 34.84	4.856 ± 0.004	4.706 ± 0.093	with
	0.5	0.00 ± 0.00	81.13 ± 13.64	6.002 ± 0.006	4.875 ± 0.170	with
	1.0	0.00 ± 0.00	79.08 ± 0.70	5.997 ± 0.002	4.848 ± 0.162	with
	2.0	0.00 ± 0.00	93.65 ± 8.72	5.990 ± 0.003	4.938 ± 0.097	with
30	0.0	85.34 ± 29.75	205.48 ± 39.31	4.981 ± 0.039	4.844 ± 0.019	with
	0.1	0.00 ± 0.00	189.65 ± 26.73	6.008 ± 0.002	4.433 ± 0.051	with
	0.5	0.00 ± 0.00	266.33 ± 55.37	6.008 ± 0.004	4.781 ± 0.143	with
	1.0	0.00 ± 0.00	94.72 ± 27.62	6.000 ± 0.003	4.917 ± 0.158	with
	2.0	0.00 ± 0.00	643.37 ± 64.95	5.798 ± 0.016	4.972 ± 0.042	with
40	0.0	79.23 ± 34.80	911.81 ± 313.20	5.022 ± 0.277	4.508 ± 0.390	with
	0.1	239.74 ± 7.65	326.25 ± 15.37	5.124 ± 0.048	4.732 ± 0.091	with
	0.5	0.00 ± 0.00	50.82 ± 6.82	6.012 ± 0.005	5.183 ± 0.078	without
	1.0	266.89 ± 39.00	1289.47 ± 128.20	5.120 ± 0.018	4.770 ± 0.165	with
	2.0	261.54 ± 40.44	315.85 ± 20.35	5.145 ± 0.047	5.005 ± 0.083	with
50	0.0	0.00 ± 0.00	602.06 ± 299.20	6.003 ± 0.004	4.751 ± 0.061	with
	0.1	0.00 ± 0.00	227.08 ± 6.01	6.008 ± 0.006	5.295 ± 0.037	without
	0.5	342.45 ± 95.02	1238.42 ± 238.40	5.184 ± 0.072	4.926 ± 0.438	with
	1.0	311.03 ± 175.30	1266.74 ± 539.30	5.158 ± 0.513	4.756 ± 0.065	with
	2.0	203.68 ± 114.40	1030.09 ± 25.82	5.187 ± 0.059	4.978 ± 0.099	with

Table 2
The data on hydrate formation kinetics in various water cuts of OW systems, both with and without hydrophobic nano-$CaCO_3$, were collected at 3 °C and 6 MPa. The standard deviation is used to represent the uncertainty of data.

Water cut, %	Concentration, wt%	t_1, min	t_2, min	P_1, MPa	P_2, MPa	With/without hydrate
10	0.0	0.00 ± 0.00	84.22 ± 3.01	6.000 ± 0.004	4.752 ± 0.012	with
	0.1	0.00 ± 0.00	139.82 ± 10.48	6.001 ± 0.003	4.809 ± 0.015	with
	0.5	0.00 ± 0.00	105.30 ± 9.27	6.008 ± 0.006	4.917 ± 0.009	without
	1.0	0.00 ± 0.00	97.62 ± 8.03	6.003 ± 0.005	4.904 ± 0.001	without
	2.0	0.00 ± 0.00	115.93 ± 11.02	6.002 ± 0.004	4.905 ± 0.003	without
20	0.0	179.72 ± 25.26	233.45 ± 49.98	4.894 ± 0.048	4.806 ± 0.047	with
	0.1	0.00 ± 0.00	98.18 ± 10.36	6.000 ± 0.003	4.967 ± 0.003	with
	0.5	738.87 ± 59.42	957.97 ± 174.50	4.979 ± 0.027	4.404 ± 0.380	with
	1.0	0.00 ± 0.00	111.85 ± 5.13	5.997 ± 0.001	5.072 ± 0.019	without
	2.0	0.00 ± 0.00	114.40 ± 6.20	5.994 ± 0.001	5.091 ± 0.022	without
30	0.0	85.34 ± 29.75	205.48 ± 39.31	4.981 ± 0.039	4.844 ± 0.019	with
	0.1	91.48 ± 34.68	384.00 ± 61.89	4.974 ± 0.045	4.422 ± 0.296	with
	0.5	166.35 ± 55.88	1329.57 ± 241.30	5.010 ± 0.253	4.188 ± 0.333	with
	1.0	146.48 ± 13.58	538.16 ± 49.94	5.078 ± 0.028	4.516 ± 0.023	with
	2.0	72.10 ± 34.21	1065.30 ± 256.40	5.074 ± 0.411	4.388 ± 0.412	with
40	0.0	79.23 ± 34.80	911.81 ± 313.20	5.022 ± 0.277	4.508 ± 0.390	with
	0.1	423.75 ± 62.46	1288.63 ± 195.30	5.005 ± 0.204	4.511 ± 0.301	with
	0.5	0.00 ± 0.00	76.46 ± 6.97	6.006 ± 0.011	5.130 ± 0.010	without
	1.0	547.19 ± 126.08	1291.56 ± 2.91	5.167 ± 0.006	4.426 ± 0.417	with
	2.0	0.00 ± 0.00	2138.25 ± 251.40	6.017 ± 0.019	3.880 ± 0.291	with
50	0.0	0.00 ± 0.00	602.06 ± 299.20	6.003 ± 0.004	4.751 ± 0.061	with
	0.1	129.78 ± 69.94	767.75 ± 353.40	5.194 ± 0.056	4.241 ± 0.209	with
	0.5	233.20 ± 119.80	930.28 ± 191.10	5.188 ± 0.093	4.187 ± 0.355	with
	1.0	0.00 ± 0.00	138.48 ± 29.96	5.991 ± 0.009	5.252 ± 0.029	without
	2.0	0.00 ± 0.00	1148.12 ± 342.30	6.004 ± 0.003	4.747 ± 0.153	with

systems is conducted by calculating three key kinetic parameters: induction time, hydrate formation amount, and average formation rate. These parameters are derived from the average values for each experiment set, as presented in Tables 1 and 2.

The induction time for each experiment group is directly available in Tables 1 and 2, with a comparative analysis shown in Fig. 5. Fig. 5 highlights the induction times for OW systems both with and without hydrophilic and hydrophobic nano-$CaCO_3$ particles. Without nanoparticles, the induction times for hydrate formation in OW systems with water cuts of 50%, 40%, 30%, 20%, and 10% are 0, 79.23, 85.34, 179.72, and 0 min, respectively. This indicates that the induction time first increases and then decreases as the water cut drops. This trend can be ascribed to the enhanced interfacial contact in the presence of the oil phase, which provides a large number of sites for heterogeneous hydrate nucleation. Nevertheless, as the volume fraction of the oil phase rises (that is, as the water cut declines), the induction time becomes longer, probably because of the decreased availability of water molecules needed for hydrate nucleation. Interestingly, when the water cut decreases further from 20% to 10%, the water molecules are more finely dispersed in the oil phase under agitation, allowing rapid formation of hydrate nucleus. This confirms that the oil phase

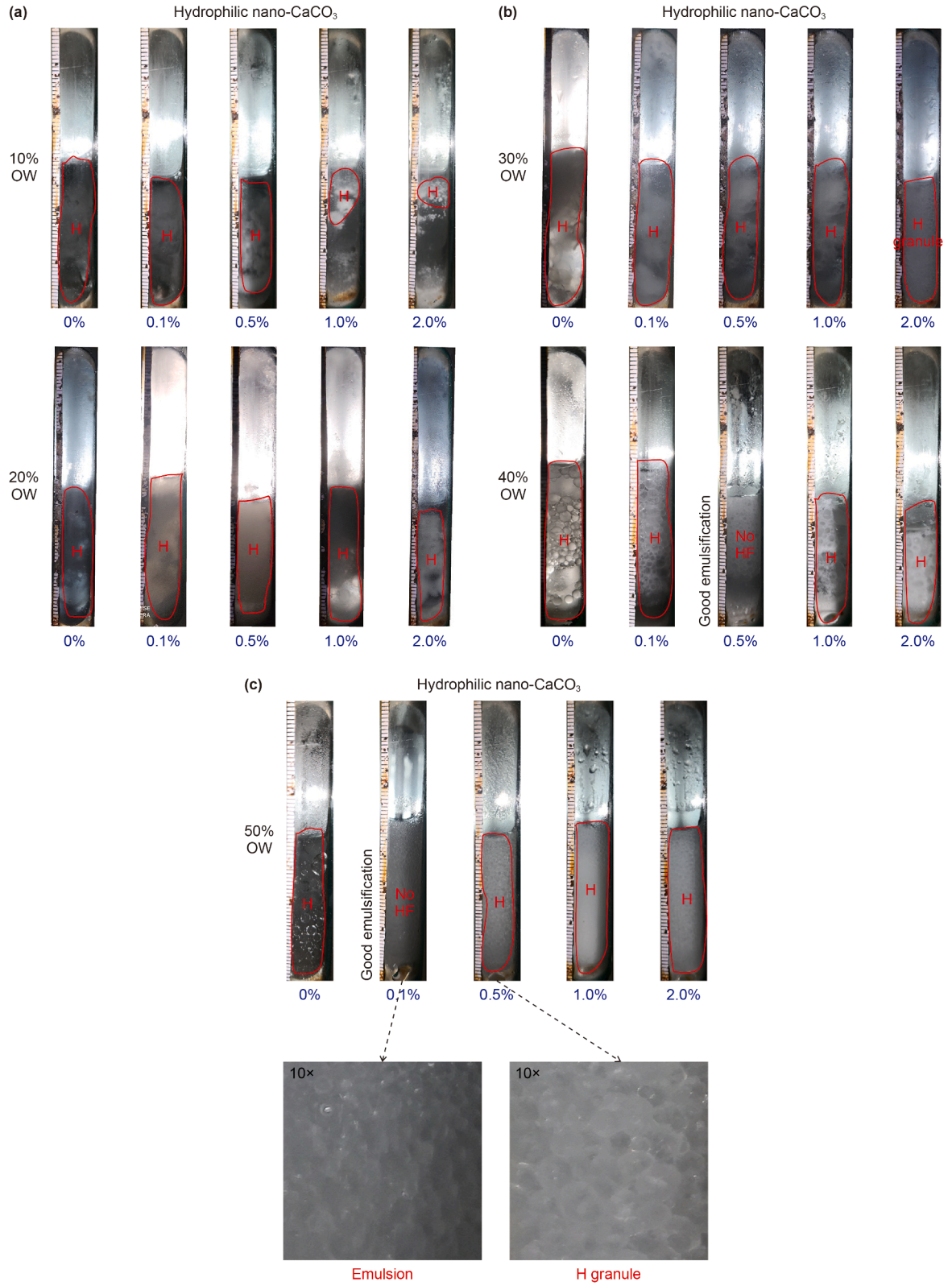

Fig. 3. The influence of hydrophilic nano-$CaCO_3$ on hydrate formation and agglomeration across various water cuts in OW systems at 3 °C and 6 MPa is depicted as follows: **(a)** 10% and 20% OW; **(b)** 30% and 40% OW; **(c)** 50% OW. "H" denotes the presence of hydrates, while "No HF" indicates the absence of hydrate formation.

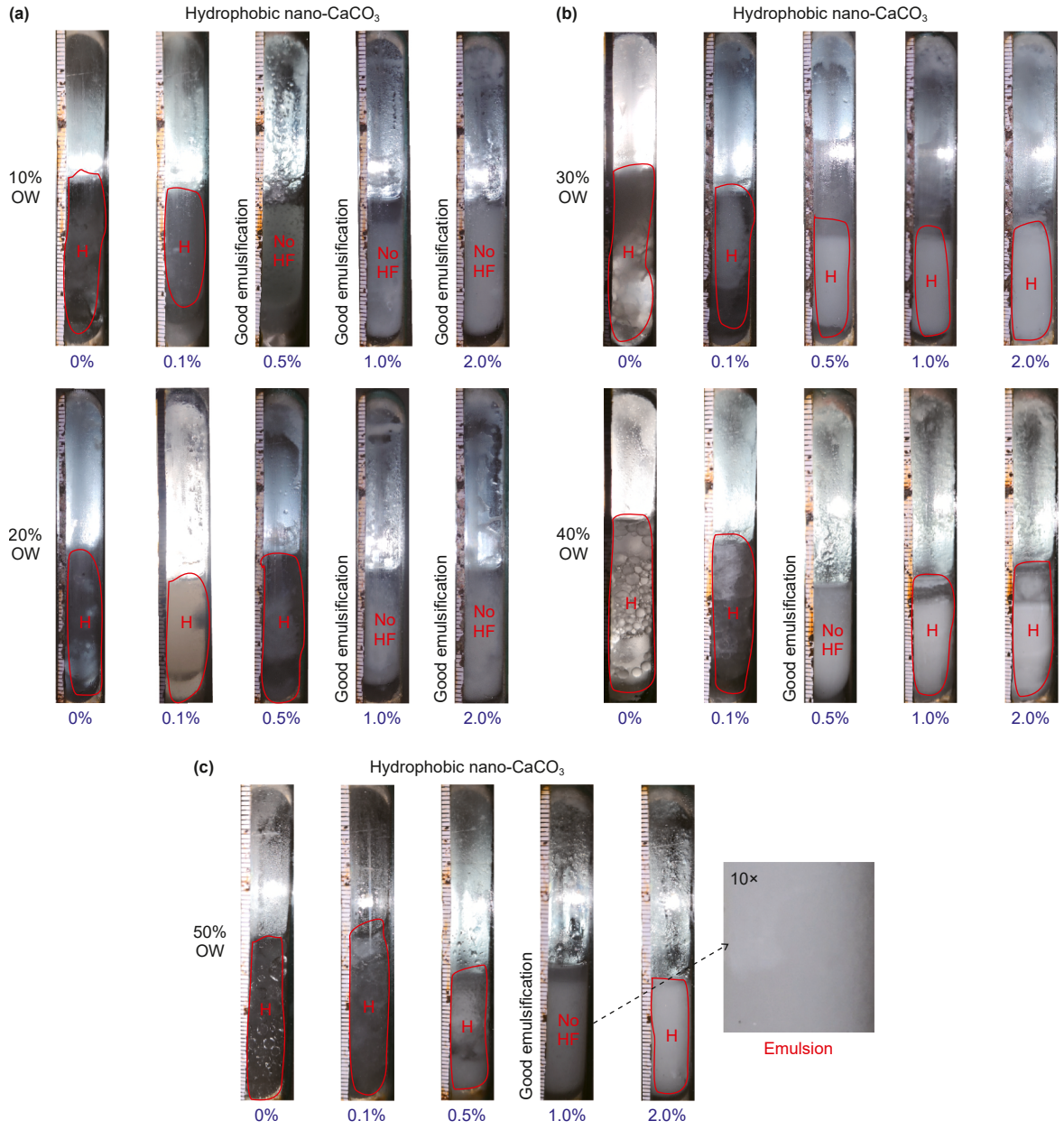

Fig. 4. The influence of hydrophobic nano-$CaCO_3$ on hydrate formation and agglomeration in various water cuts of OW systems at 3 °C and 6 MPa is illustrated as follows: **(a)** 10% and 20% OW; **(b)** 30% and 40% OW; **(c)** 50% OW. "H" indicates the presence of hydrates, while "No HF" signifies the absence of hydrate formation.

volume fraction (or water cut) plays a critical role in hydrate formation in OW systems (Ning et al., 2022).

When hydrophilic nano-$CaCO_3$ particles are introduced into OW systems, the induction time of hydrate formation changes based on both the nanoparticle concentration (0.1, 0.5, 1.0, and 2.0 wt%) and the water cut. In the 10% OW system, the 0.5 wt% concentration of hydrophilic nano-$CaCO_3$ particles inhibits hydrate nucleation, but this inhibitory effect diminishes at other concentrations. As the water cut increases to 20% and 30%, the particles tend to promote hydrate nucleation, often resulting in an induction time of 0 min in most cases. However, in systems with higher water cuts of 40% and 50%, hydrophilic nano-$CaCO_3$ prolongs the induction time and can even completely prevent hydrate nucleation in certain cases (e.g., 40% OW + 1.0 wt%, 50% OW + 0.5 wt%) (Fig. 5(a)).

The variations in induction time across different OW systems likely stem from the interplay between nanoparticles and the OW interface. Firstly, a specific concentration of both hydrophilic and hydrophobic nano-$CaCO_3$ particles can significantly influence hydrate nucleation in a pure water system (Guo et al., 2022). Moreover, the distribution of the oil and water phases influenced by different water cuts, and the localization of nanoparticles at the OW interface, can further affect the system's overall ability to inhibit hydrate nucleation (Baek et al., 2015). Observations during the experiments (Figs. 3 and 6(a)) and reveal that systems with stronger inhibition properties typically exhibit improved emulsification. Previous studies have shown that small solid particles, including nanoparticles, can act as effective emulsifiers. Hydrophilic nanoparticles tend to form O/W emulsions in OW systems, while hydrophobic nanoparticles favor the formation of W/O

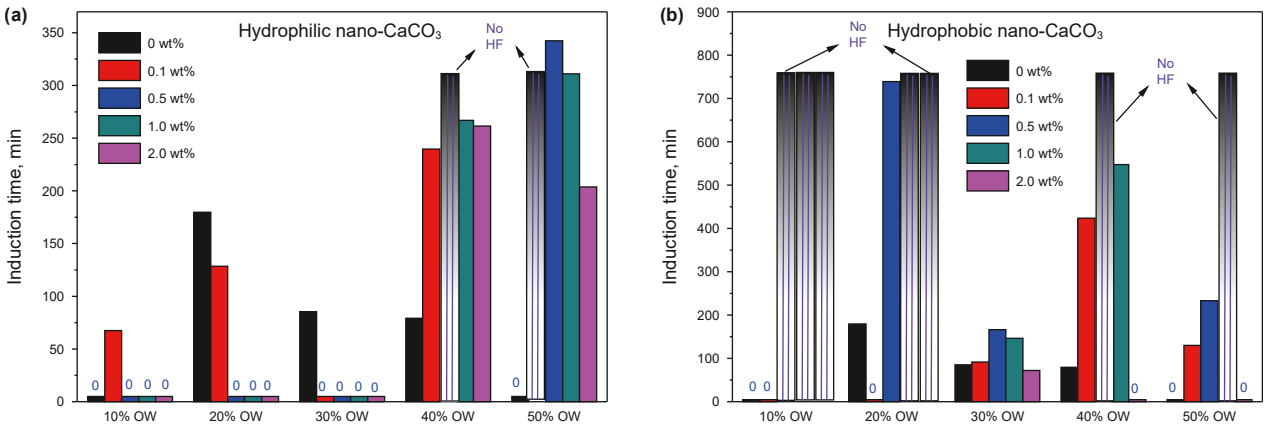

Fig. 5. Induction time for hydrate formation in each set of experiment. **(a)** OW systems with varying water cuts containing hydrophilic nano-$CaCO_3$; **(b)** OW systems with varying water cuts containing hydrophobic nano-$CaCO_3$. The lined vertical bar signifies the absence of hydrate formation, with "No HF" denoting that no hydrates were formed, and it does not represent any specific induction time. For clarity, instances of 0 min induction time have been displayed as 5 min. Initial temperature and pressure conditions are set to 3 °C and 6 MPa.

emulsions (Gavrielatos et al., 2019). Therefore, enhancing the emulsification of OW systems is key to utilizing nano-$CaCO_3$ particles for inhibiting hydrate formation.

Further analysis indicates that hydrophilic nano-$CaCO_3$ particles exhibit a stronger inhibitory effect in systems with higher water cuts, which is attributed to their dispersion within the water and oil phases and their coverage density at the OW interface (Fig. 7). The majority of hydrophilic nano-$CaCO_3$ particles distribute within the aqueous phase and accumulate at the OW interface. Their arrangement at the interface is influenced by stirring, the order of sample preparation, and particle concentration. When the water cut is high (e.g., 40% and 50%), OW systems tend to form O/W emulsions under appropriate conditions (Fig. 6(a)). As demonstrated in earlier studies (Guo et al., 2022), hydrophilic nano-$CaCO_3$ particles can inhibit hydrate nucleation in the water phase. If these particles form a dense layer at the OW interface, it further suppresses hydrate nucleation. In systems with lower water cuts (e.g., 10% and 20%), however, hydrophilic nano-$CaCO_3$ particles may fail to form a dense layer at the interface (Fig. 7(b)). Instead, under stirring conditions, they can disrupt the OW interface, lower the interfacial tension, and boost hydrate nucleation. Additionally, the concentration of nanoparticles affects their density at the interface and the overall emulsification process. These complex interactions and cumulative effects likely explain the varying impacts of hydrophilic nano-$CaCO_3$ particles on hydrate nucleation in OW systems.

When varying concentrations of hydrophobic nano-$CaCO_3$ particles (0.1, 0.5, 1.0, and 2.0 wt%) are introduced into the OW system, most cases (except for 20% OW + 0.1 wt%; 30% OW + 2.0 wt%) show that these nanoparticles inhibit hydrate nucleation, resulting in prolonged induction times. Notably, in certain instances, such as 10% OW systems combined with 0.5, 1.0, and 2.0 wt% concentrations, hydrate formation is entirely suppressed (Fig. 5(b)). The data indicate that lower water cuts and higher concentrations of hydrophobic nanoparticles enhance the inhibition effect on hydrate nucleation. Observations from Fig. 4 and the experimental process (Fig. 6(b)) reveal that systems exhibiting stronger inhibition also demonstrate superior emulsification, as illustrated in Fig. 4(c). Thus, enhancing emulsification is crucial for utilizing hydrophobic nano-$CaCO_3$ particles to prevent hydrate formation and agglomeration in OW systems.

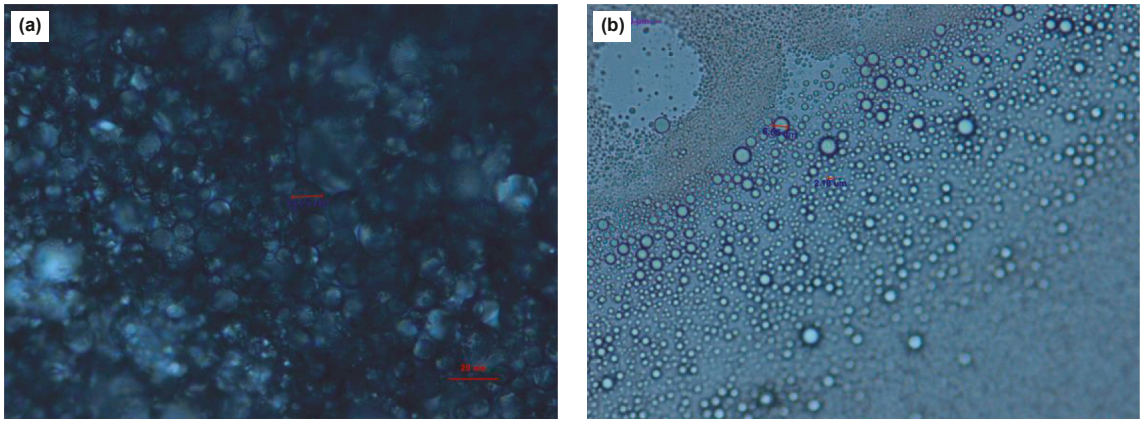

Fig. 6. Optical microscope pictures (50×) of Pickering emulsion formed by hydrophilic and hydrophobic nanoparticles: **(a)** 50% OW system with 0.5 wt% hydrophilic nano-$CaCO_3$, where hydrophilic nanoparticles stabilize the O/W emulsion by dispersing within the water phase and enhancing the stability of the oil-water interface; **(b)** 50% OW system with 0.5 wt% hydrophobic nano-$CaCO_3$, showing a W/O emulsion where hydrophobic nanoparticles reside predominantly in the oil phase, stabilizing the dispersed water droplets.

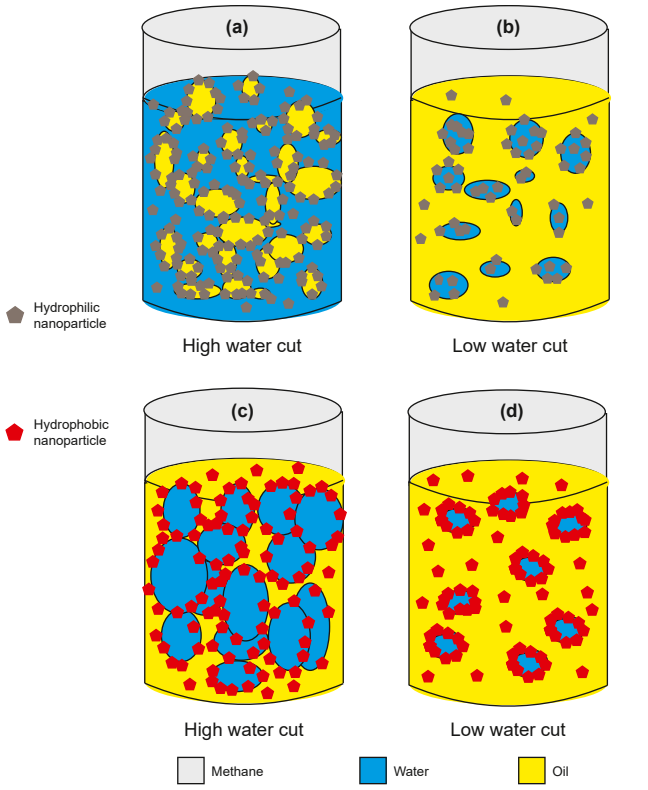

Fig. 7. Mechanism diagram of the distribution of hydrophilic and hydrophobic nanoparticles in OW systems with different water cuts. **(a)** Hydrophilic nanoparticles in high water cut system; **(b)** hydrophilic nanoparticles in low water cut system; **(c)** hydrophobic nanoparticles in high water cut system; **(d)** hydrophobic nanoparticles in low water cut system.

Furthermore, these hydrophobic nanoparticles exhibit better emulsification at low water cuts, which relates to their distribution within the water and oil phases, as well as their coverage at the OW interface (Fig. 7(d)). At lower water cuts, the OW system forms a water-in-oil (W/O) Pickering emulsion under the influence of hydrophobic nanoparticles. This emulsion effectively reduces interfacial tension and establishes a dense interfacial film (Chevalier and Bolzinger, 2013; Gavrielatos et al., 2019). This configuration hinders methane gas diffusion into the aqueous phase and physically obstructs hydrate crystal formation by occupying nucleation sites, thereby inhibiting hydrate formation.

Conversely, at higher water cuts, the same concentration of hydrophobic nanoparticles does not lead to the formation of a closed-packed adsorbed layer at the interface (Fig. 7(c)). The resulting W/O emulsion may lack stability, leading to a weaker inhibition effect on hydrate nucleation. Additionally, while hydrophobic nano-$CaCO_3$ particles may not inhibit hydrate formation at higher water cuts, the emulsification improves with increasing nanoparticle concentration, preventing large agglomerations even if hydrate is formed (Fig. 4). Instead, small hydrate particles remain dispersed in the oil phase, which contributes to the overall stability of the OW systems and mitigates potential hazards in practical applications.

4.2. Amount of hydrate formation

Consistent with our previous research (Ning et al., 2022), some systems exhibit no hydrate formation under specific water cut conditions, while others do form hydrates with distinct induction times (see Tables 1 and 2; Figs. 3 and 4). Consequently, in the absence of hydrate formation, the final equilibrium pressure is defined as the equilibrium pressure for gas solubility. Moreover, the equilibrium pressure at the end of the induction phase can also be regarded as the equilibrium pressure for gas solubility. Subsequently, the amounts of saturated dissolved CH_4 in different water-cut systems can be determined by using the equation of state specific to each system (Table 3). Therefore, ignoring the influence of hydrophilic and hydrophobic nanoparticles on the solubility of CH_4 molecules, the amounts of hydrate formation (Fig. 8) in different water cuts of OW systems—whether containing hydrophilic and hydrophobic nano-$CaCO_3$ or not—can be determined using Eq. (1) and Table 3.

It can be concluded that, in the absence of any nano-$CaCO_3$ particles, the amount of hydrate formation initially increases with the water cut but experiences a slight decrease once the water cut reaches 50% (Fig. 8). This trend is primarily influenced by the varying water cuts of different OW systems. For instance, the water volume in a 40% OW system is double that in a 20% OW system. However, when the water cut reaches a certain threshold, the system may transition from a W/O to an O/W configuration. The hydrate that forms initially can impede subsequent hydrate formation, potentially reducing the conversion of water to hydrate. Consequently, the amount of hydrate formation in the 50% OW system is marginally lower than in the 40% OW system, but the likelihood of hydrate blockage remains significant.

When hydrophilic nano-$CaCO_3$ particles at various concentrations (0.1, 0.5, 1.0, and 2.0 wt%) are added to the OW systems (Fig. 8 (a)), distinct trends in hydrate formation are observed. At low concentrations (0.1 wt%), the addition of hydrophilic nano-$CaCO_3$ enhances hydrate formation in 10% and 20% water cut systems. However, at higher concentrations (0.5–2.0 wt%), these particles reduce the amount of hydrate formation. Similarly, in the 30% OW system, low concentrations (0.1 and 0.5 wt%) promote hydrate formation, while higher concentrations (1.0 and 2.0 wt%) inhibit it. In systems with high water cuts (40% and 50%), the presence of hydrophilic nano-$CaCO_3$ reduces the amount of hydrate formation in comparison to systems without these nanoparticles. In some instances, such as 40% OW with 1.0 wt% and 50% OW with 0.5 wt%, hydrate formation is completely suppressed (Fig. 8(a)). This promotion of hydrate conversion at lower concentrations may result from the disruption of initial hydrate shells if the emulsification is poor, allowing better contact between water and gas. Conversely, the steric hindrance of nanoparticles at the OW interface (Fig. 7), along with similar inhibition mechanisms observed in pure water systems (Guo et al., 2022), leads to decreased hydrate formation. Further analysis indicates that the inhibitory effect of hydrophilic nano-$CaCO_3$ particles on hydrate formation is more pronounced at higher water cuts, paralleling the observations for induction time.

Therefore, compared with the system with poor emulsification effect, the proportion of water phase converted to hydrate in OW system with good emulsification is higher. However, when the water cut is low, it is difficult to destroy the interfacial film even the hydrate is formed. The nanoparticle film can still form a steric hindrance to prevent further hydrate formation.

Except in cases where hydrate formation is completely prevented (e.g., 10% OW with 0.5, 1.0, and 2.0 wt%), hydrophobic nano-$CaCO_3$ particles tend to promote hydrate formation amount in OW systems with high water cuts (30%, 40%, and 50%). Conversely, in lower water cut systems (10% and 20%), even if hydrates form, hydrophobic nanoparticles generally reduce the amount of hydrate produced (Fig. 8(b)). This behavior may arise because

Table 3
At 3 °C and 6 MPa, the saturated dissolved CH_4 quantities in various water cuts of OW systems (both those with hydrophilic and hydrophobic nanoparticles and those without) were computed by means of the equation of state unique to each system.

Various water cuts of OW systems	50% OW	40% OW	30% OW	20% OW	10% OW
Pressure at equilibrium of CH_4 dissolution, MPa	5.111	5.022	4.981	4.879	4.864
The saturated dissolved CH_4 amounts, mol	0.184	0.202	0.210	0.227	0.234

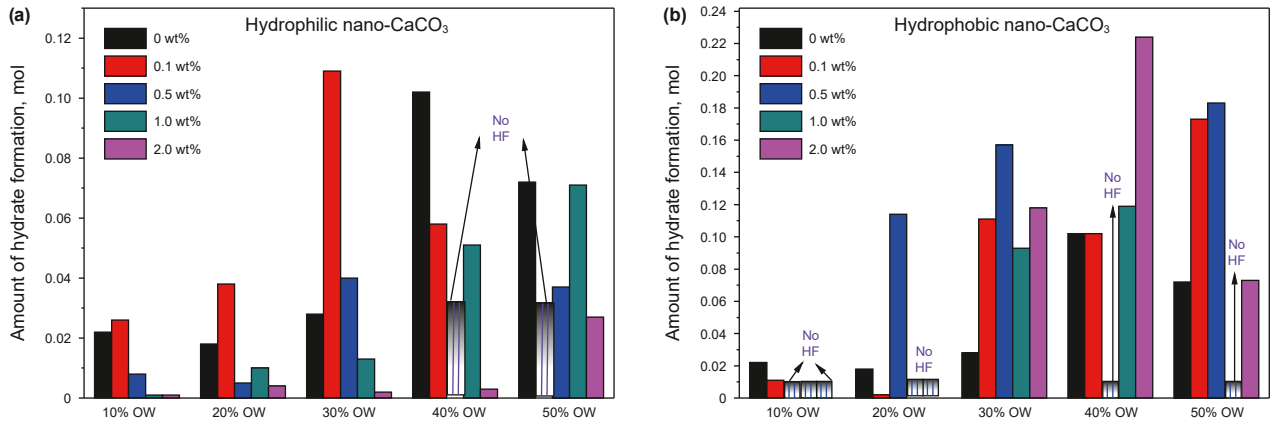

Fig. 8. The amount of hydrate formation in each set of experiment is shown as follows: **(a)** various water cuts in OW systems with hydrophilic nano-$CaCO_3$; **(b)** various water cuts in OW systems with hydrophobic nano-$CaCO_3$. The lined vertical bar represents that no hydrate formation has occurred and does not denote a specific quantity of hydrate (where "No HF" stands for no hydrate formation having taken place). The initial temperature and pressure conditions were set at 3 °C and 6 MPa.

hydrophobic nanoparticles can emulsify the OW systems, creating dense films at the interface. Once hydrates form, these interfacial films can easily break, releasing water from the dispersed phase, which then facilitates further hydrate formation (Guo et al., 2020). Additionally, since hydrophobic nanoparticles can enhance hydrate formation in pure water, they similarly promote hydrate formation at high water cuts (Guo et al., 2022). The internal water phase is more effectively dispersed within the oil phase due to nanoparticle emulsification, leading to a higher proportion of water converting to hydrates in well-emulsified OW systems. However, at low water cuts, the interfacial film is less likely to break, even with hydrate formation. In these cases, the nanoparticle film continues to provide steric hindrance, inhibiting further hydrate formation.

4.3. The average hydrate growth rate

Fig. 9 illustrates the average hydrate growth rate in OW systems with varying water cuts at 3 °C and 6 MPa, both with and without the addition of hydrophilic and hydrophobic nano-$CaCO_3$ particles. The findings indicate that, in systems lacking nano-$CaCO_3$, a lower water cut corresponds to a faster rate of hydrate formation. This phenomenon occurs because the introduction of a specific volume of oil phase significantly increases the interfacial area. As a result, more nucleation sites are created and the mass transfer process is enhanced, thus speeding up the rate of hydrate growth.

When hydrophilic nano-$CaCO_3$ particles at various concentrations (0.1, 0.5, 1.0, and 2.0 wt%) are introduced into OW systems, the hydrate formation rate generally decreases compared to the

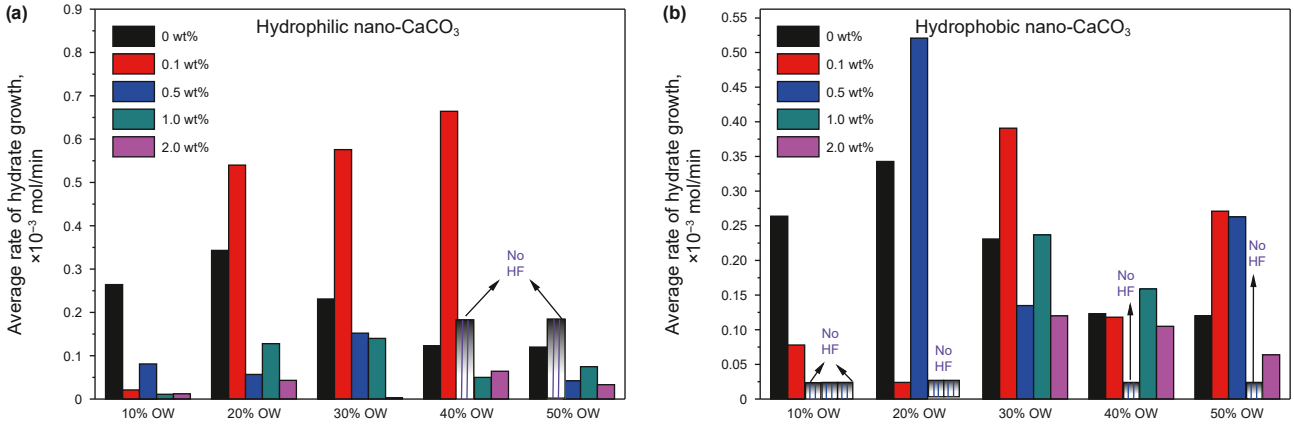

Fig. 9. The average hydrate growth rate in each experimental set is presented as follows: **(a)** various water cuts of OW systems with added hydrophilic nano-$CaCO_3$; **(b)** various water cuts of OW systems with added hydrophobic nano-$CaCO_3$. The striped vertical bars indicate no hydrate formation and should not be interpreted as representing the formation of any number of hydrates ("No HF" signifies no hydrate formation). The initial experimental conditions were a temperature of 3 °C and a pressure of 6 MPa.

pure OW system without nanoparticles. In certain cases, hydrate formation is entirely prevented (e.g., 40% OW with 1.0 wt%; 50% OW with 0.5 wt%) (Fig. 9(a)). However, the addition of 0.1 wt% hydrophilic nano-$CaCO_3$ particles promotes the hydrate formation rate in systems with medium water cuts (20%–40%), whereas higher concentrations (0.5–2.0 wt%) lead to a reduced formation rate. The underlying inhibition and promotion mechanisms are consistent with those discussed in previous sections (4.1 and 4.2). Further analysis also indicates that hydrophilic nano-$CaCO_3$ particles exhibit stronger inhibitory effects on hydrate formation at higher water cuts and higher concentrations.

When hydrophobic nano-$CaCO_3$ particles at varying concentrations are introduced into the OW systems (Fig. 9(b)), their overall effect on the hydrate growth rate at high water cuts (30%–50% OW) is less pronounced, with some systems showing hydrate promotion while others exhibit inhibition. At lower water cuts (10% and 20%), hydrophobic nanoparticles generally reduce the hydrate growth rate. However, in certain cases, such as 20% OW with 0.5 wt%, the nucleation of hydrates disrupts the OW interface, leading to a rapid acceleration in hydrate growth due to the presence of hydrophobic nanoparticles. The mechanisms underlying these inhibition and promotion effects align with those discussed previously, though the balance between these effects can vary depending on system parameters. Hydrophobic nano-$CaCO_3$ particles tend to show stronger inhibition on hydrate growth rates at low water cuts and higher concentrations. This is likely due to particle saturation at the interface, where nanoparticles aggregate and form a stable, thick layer on the W/O emulsion (Baek et al., 2019). The oil film becomes occupied by nanoparticles differently at low and high concentrations, contributing to the observed retardation or enhancement in hydrate formation.

Based on the results, it can be deduced that in the absence of nano-$CaCO_3$ particles, hydrates form and aggregate readily in OW systems, whether the water cut is high or low, potentially leading to negative impacts on flow assurance and production operations. However, the introduction of various concentrations of hydrophilic nano-$CaCO_3$ particles inhibits hydrate formation in most cases, and in some instances (40% OW + 1.0 wt%; 50% OW + 0.5 wt%), hydrate formation is completely prevented. The data suggest that hydrophilic nano-$CaCO_3$ particles exhibit stronger inhibition effects at higher water cuts and concentrations. Similarly, hydrophobic nano-$CaCO_3$ particles can also inhibit hydrate formation under specific conditions, with their inhibitory effect being more pronounced at lower water cuts. While the concentration of nanoparticles affects the experimental outcomes, the trend is not entirely consistent. Therefore, by selecting the appropriate type and concentration of nanoparticles based on specific conditions (e.g., water cut), it is possible to effectively inhibit hydrate formation and aggregation.

4.4. Limitations and future work

The type (composition) of oil can significantly influence the system's ability to inhibit hydrate formation and agglomeration, and many studies have corroborated this viewpoint (Almashwali et al., 2022; Daraboina et al., 2015; Fadnes, 1996; Meng et al., 2025). Crude oil is a complex mixture, primarily composed of alkanes, aromatic hydrocarbons, asphaltenes, and other colloidal compounds (Meng et al., 2025). Research indicates that the ability of crude oils to form hydrate plugs can vary greatly, mainly due to the presence of polar components (such as resins and asphaltenes), which have been shown to inhibit hydrate formation and aggregation (Fadnes, 1996). The inhibition potential varies depending on the crude oil type, likely due to a combination of different inhibition mechanisms, and possibly due to competition between inhibitive and promotive effects (Daraboina et al., 2015; Meng et al., 2025). Additionally, oil components with small particle sizes and charged surfaces can interact with nanoparticles through adsorption or electrostatic forces (Arab et al., 2018; Talatori and Barth, 2011). Surface-active molecules present in the oil may modify interfacial tension and nanoparticle wettability, thereby affecting their distribution in both the bulk phase and at OW interface. These interactions can destabilize the interface, compromising the effectiveness of nanoparticles and the overall system in mitigating hydrate formation and aggregation (Chen et al., 2019; Guo et al., 2024; Talatori and Barth, 2011).

The selection of mineral oil was based on its chemical stability, low volatility, excellent lubricating properties, and its ability to facilitate clear observation of experimental phenomena. While the current work primarily investigates the effects of nanoparticles on hydrate formation and agglomeration in OW systems, it is acknowledged that incorporating a broader range of oil compositions is essential to improve the generalizability of the findings. To this end, future studies will explore the influence of different oil compositions on hydrate inhibition behavior using both macroscopic and microscopic evaluation methods. Furthermore, the present study considers key variables known to affect hydrate formation and aggregation in OW systems, including water cut (10%–50%) and nanoparticle concentration (0.1, 0.5, 1.0, and 2.0 wt%), to examine their impact on experimental outcomes. However, the current analysis primarily emphasizes kinetic behavior and trend observations. The underlying mechanisms through which these factors influence hydrate inhibition remain insufficiently understood and warrant further investigation (Fig. 10).

Building on the current research, future investigations will examine the effects of various factors, including water cut (5%–100%), oil composition, water salinity, nanoparticle properties (such as type, particle size, and wettability), and the emulsification process (e.g., stirring rate and addition sequence), on the distribution and relative positioning of oil, water, and nanoparticles within the system (Fig. 10(a) and (b)). These factors will be studied in depth to elucidate their influence on emulsion type (W/O or O/W), OW interface stability, and overall system stability (Fig. 10(c)). Ultimately, a relationship will be established between emulsion system properties (e.g., kinetics inhibition and anti-agglomeration efficiency) and the aforementioned influencing factors, thereby enabling parameter optimization for enhanced hydrate inhibition performance (Fig. 10).

To determine emulsion type and phase distribution, dye-tracing techniques combined with microscopic imaging will be employed, with particular emphasis on identifying threshold conditions (e.g., critical water cut or nanoparticle concentration) that induce phase inversion. Emulsion stability will be evaluated through both qualitative observations and quantitative analyses, including droplet size distribution and demulsification voltage measurements. Although capturing dynamic changes during hydrate formation remains challenging due to experimental limitations, emphasis will be placed on analyzing emulsion stability prior to hydrate formation and following dissociation (Fig. 10(c)). Furthermore, to gain deeper insights into the underlying inhibition mechanisms, a combination of macroscopic experiments, microscopic imaging, and molecular dynamics (MD) simulations will be utilized to investigate the interactions among oil, water, nanoparticles, and gas molecules (Fig. 10(b)).

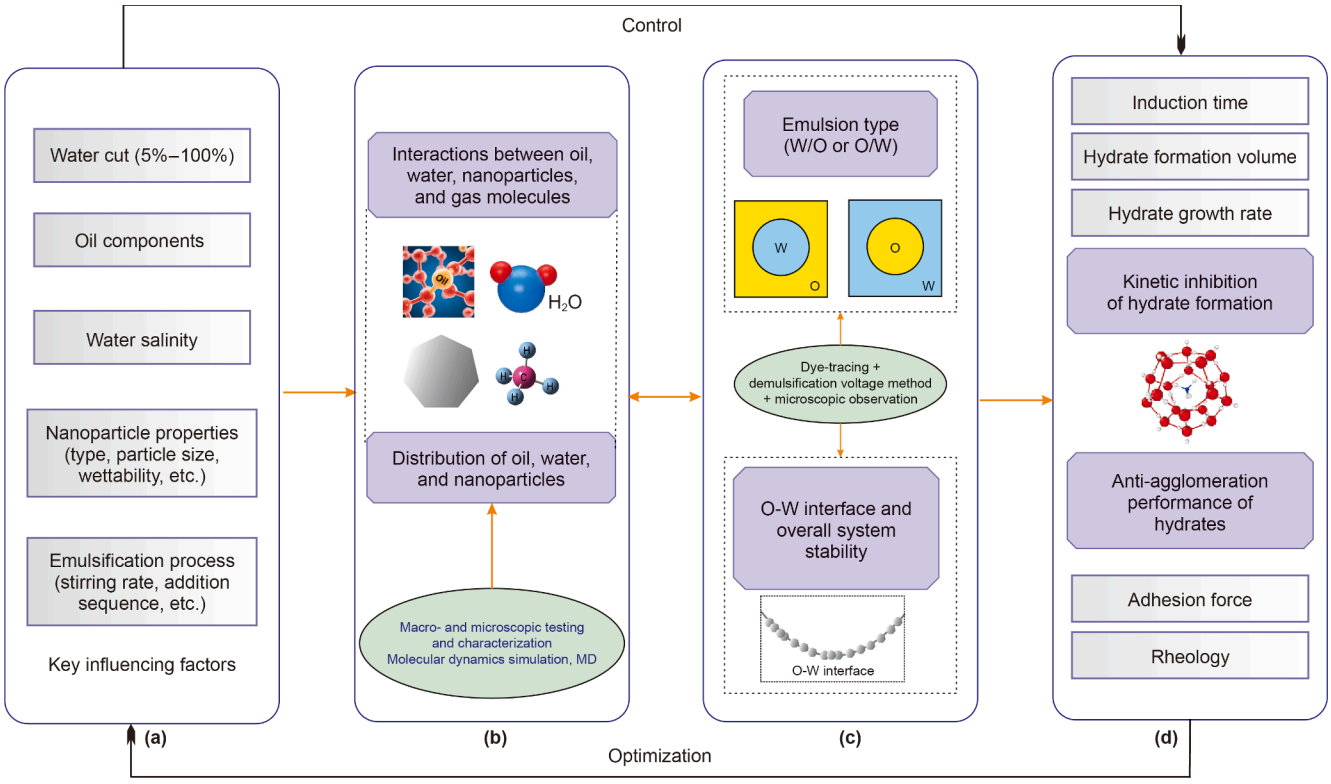

Fig. 10. Schematic of the comprehensive study on the influence and mechanisms of nanoparticles on hydrate formation in OW systems. **(a)** Key influencing factors; **(b)** the distribution of oil, water, and nanoparticles in the system; **(c)** emulsion type (W/O or O/W), OW interface stability, and overall system stability; **(d)** kinetics inhibition and anti-agglomeration performance.

5. Conclusions

In this study, experiments were conducted on methane hydrate formation in OW systems, both with and without hydrophilic and hydrophobic nano-$CaCO_3$ particles, at 3 °C and 6 MPa. The results showed that in the absence of nano-$CaCO_3$ particles, hydrates readily form and aggregate in OW systems, regardless of water cut, which can negatively affect flow assurance and production processes. When hydrophilic nano-$CaCO_3$ particles were added at concentrations ranging from 0.1 to 2.0 wt%, they inhibited hydrate formation in systems with 10%–50% water cut, with complete prevention observed in certain cases (e.g., 40% OW + 1.0 wt%; 50% OW + 0.5 wt%). The inhibition effect was stronger at higher water cuts, making hydrophilic nano-$CaCO_3$ particles particularly suitable for high-water-cut systems. Hydrophobic nano-$CaCO_3$ particles also suppressed hydrate formation, with a more pronounced effect at lower water cuts, indicating their potential use in low-water-cut systems. While the concentration of nanoparticles affected the results, the pattern of this influence was not entirely consistent. This study provides valuable insight into how hydrophilic and hydrophobic nanoparticles influence methane hydrate formation and aggregation, offering a potential mechanism for their use in hydrate management during well drilling and flow assurance. Future work will focus on uncovering the molecular-scale mechanisms of these effects and exploring the combination of nanoparticles with other additives, such as anti-agglomerants (AAs), to enhance hydrate inhibition.

CRediT authorship contribution statement

Dong-Dong Guo: Writing – review & editing, Writing – original draft, Software. **Wen-Jia Ou:** Methodology. **Yun-Hong Zhang:** Visualization, Data curation. **Heng-Yin Zhu:** Supervision, Conceptualization. **Shahab Ud Din:** Investigation, Software. **Ren Wang:** Supervision, Methodology. **Fu-Long Ning:** Project administration, Funding acquisition, Supervision, Conceptualization.

Declaration of competing interest

The authors declare that they have no known competing financial interests or personal relationships that could have appeared to influence the work reported in this paper.

Acknowledgments

This work was supported by the National Natural Science Foundation of China (No. 42402319; 51704266), the Anhui Provincial Natural Science Foundation (No. 2308085QE151), the Natural Science Research Project of Anhui Educational Committee (No. 2023AH051222), Young Talent Nurturing Program of Anhui Association For Science and Technology (No. RCTJ202403), the Open Foundation of the Innovation Base of Fine Mine Prospecting and Intelligent Monitoring Technology (No. 2023-MPIM-01) and was partly supported by the Open Fund of Engineering Research Center of Rock-Soil Drilling & Excavation and Protection (No. 202407).

References

Abay, H.K., Svartaas, T.M., 2010. Effect of ultralow concentration of methanol on methane hydrate formation. Energy Fuels 24 (2), 752–757. https://doi.org/10.1021/ef9009422.
Ahmed, T.H., 1989. Hydrocarbon Phase Behavior. Guif Publishing Company, Texas.
Ahuja, A., 2015. Hydrate Forming Emulsion: Rheology and Morphology Analysis for Flow Assurance. Dissertations & Theses – Gradworks.

Ahuja, A., Iqbal, A., Iqbal, M., et al., 2018. Rheology of hydrate-forming emulsions stabilized by surfactant and hydrophobic silica nanoparticles. Energy Fuels 32 (5), 5877–5884. https://doi.org/10.1021/acs.energyfuels.8b00795.
Aliabadi, M., Rasoolzadeh, A., Esmaeilzadeh, F., et al., 2015. Experimental study of using CuO nanoparticles as a methane hydrate promoter. J. Nat. Gas Sci. Eng. 27, 1518–1522. https://doi.org/10.1016/j.jngse.2015.10.017.
Almashwali, A.A., Bavoh, C.B., Lal, B., et al., 2022. Gas hydrate in oil-dominant systems: a review. ACS Omega 7 (31), 27021–27037. https://doi.org/10.1021/acsomega.2c02278.
Aman, Z.M., Dieker, L.E., Aspenes, G., et al., 2010. Influence of model oil with surfactants and amphiphilic polymers on cyclopentane hydrate adhesion forces. Energy Fuels 24 (10), 5441–5445. https://doi.org/10.1021/ef100762r.
Aman, Z.M., Koh, C.A., 2016. Interfacial phenomena in gas hydrate systems. Chem. Soc. Rev. 45, 1–26. https://doi.org/10.1039/c5cs00791g.
Arab, D., Kantzas, A., Bryant, S.L., 2018. Nanoparticle stabilized oil in water emulsions: a critical review. J. Petrol. Sci. Eng. 163, 217–242. https://doi.org/10.1016/j.petrol.2017.12.091.
Baek, S., Min, J., Ahn, Y.H., et al., 2019. Effect of hydrophobic silica nanoparticles on the kinetics of methane hydrate formation in water-in-oil emulsions. Energy Fuels 33, 523–530. https://doi.org/10.1021/acs.energyfuels.8b03210.
Baek, S., Min, J., Lee, J.W., 2015. Inhibition effects of activated carbon particles on gas hydrate formation at oil–water interfaces. RSC Adv. 5 (72), 58813–58820. https://doi.org/10.1039/c5ra08335d.
Cha, M., Baek, S., Morris, J., et al., 2014. Hydrophobic particle effects on hydrate crystal growth at the water–oil interface. Chem. Asian J. 9 (1), 261–267. https://doi.org/10.1002/asia.201300905.
Chastain, B.K., Chevrier, V., 2007. Methane clathrate hydrates as a potential source for martian atmospheric methane. Planet. Space Sci. 55 (10), 1246–1256. https://doi.org/10.1016/j.pss.2007.02.003.
Chen, Y., Renner, P., Liang, H., 2019. Dispersion of nanoparticles in lubricating oil: a critical review. Lubricants 7 (1), 7. https://doi.org/10.3390/lubricants7010007.
Chevalier, Y., Bolzinger, M.A., 2013. Emulsions stabilized with solid nanoparticles: pickering emulsions. Colloids Surf. A Physicochem. Eng. Asp. 439, 23–34. https://doi.org/10.1016/J.COLSURFA.2013.02.054.
Chong, Z.R., Yang, S.H.B., Babu, P., et al., 2016. Review of natural gas hydrates as an energy resource: prospects and challenges. Appl. Energy 162, 1633–1652. https://doi.org/10.1016/j.apenergy.2014.12.061.
Daraboina, N., Pachitsas, S., von Solms, N., 2015. Natural gas hydrate formation and inhibition in gas/crude oil/aqueous systems. Fuel 148, 186–190. https://doi.org/10.1016/j.fuel.2015.01.103.
Deng, Z., Fan, S., Wang, Y., et al., 2023. High storage capacity and high formation rate of carbon dioxide hydrates via super-hydrophobic fluorinated graphenes. Energy 264, 126045. https://doi.org/10.1016/j.energy.2022.126045.
Fadnes, F.H., 1996. Natural hydrate inhibiting components in crude oils. Fluid Phase Equilib. 117 (1–2), 186–192. https://doi.org/10.1016/0378-3812(95)02952-4.
Farhang, F., Nguyen, A.V., Sewell, K.B., 2014. Fundamental investigation of the effects of hydrophobic fumed silica on the formation of carbon dioxide gas hydrates. Energy Fuels 28, 7025–7037. https://doi.org/10.1021/ef5009133.
Gavrielatos, I., Dabirian, R., Mohan, R.S., et al., 2019. Oil/water emulsions stabilized by nanoparticles of different wettabilities. J. Fluid Eng. 141 (2), 021301. https://doi.org/10.1115/1.4040465.
Guo, D.D., Ou, W.J., Ning, F.L., et al., 2020. The effects of hydrate formation and dissociation on the water-oil interface: insight into the stability of an emulsion. Fuel 266, 116980. https://doi.org/10.1016/j.fuel.2019.116980.
Guo, D.D., Ou, W.J., Ning, F.L., et al., 2022. Effects of hydrophilic and hydrophobic nano-$CaCO_3$ on kinetics of hydrate formation. Energy Sci. Eng. 10 (5), 1–18. https://doi.org/10.1002/ese3.1042.
Guo, D.D., Sun, J.X., Yao, J.J., et al., 2024. Hydrate Formation and agglomeration in the compound of hydrophilic nano-$CaCO_3$ and inhibitors. Energy Fuels 38, 16385–16397. https://doi.org/10.1021/acs.energyfuels.4c02882.
Hammerschmidt, E.G., 1934. Formation of gas hydrates in natural gas transmission lines. Ind. Eng. Chem. 26 (8), 851–855. https://doi.org/10.1021/ie50296a010.
Kakati, H., Mandal, A., Laik, S., 2016. Promoting effect of Al_2O_3/ZnO-based nanofluids stabilized by SDS surfactant on CH_4+C_2H_6+C_3H_8 hydrate formation. J. Ind. Eng. Chem. 38, 130–138. https://doi.org/10.1016/j.jiec.2016.01.014.
Kar, S., Kakati, H., Mandal, A., et al., 2016. Experimental and modeling study of kinetics for methane hydrate formation in a crude oil-in-water emulsion. Pet. Sci. 13, 489–495. https://doi.org/10.1007/s12182-016-0108-3.
Kashchiev, D., Firoozabadi, A., 2003. Induction time in crystallization of gas hydrates. J. Cryst. Growth 250 (3/4), 499–515. https://doi.org/10.1016/S0022-0248(02)02461-2.
Lachance, J.W., Sloan, E.D., Koh, C.A., 2008. Effect of hydrate formation/dissociation on emulsion stability using DSC and visual techniques. Chem. Eng. Sci. 63 (15), 3942–3947. https://doi.org/10.1016/j.ces.2008.04.049.
Lim, S.G., Oh, C.Y., Lee, J.W., et al., 2023. Sustainable freshwater recovery from radioactive wastewater by gas hydrate formation. Chem. Eng. J. 461, 141830. https://doi.org/10.2139/ssrn.4306042.
Ma, Z.W., Zhang, P., Bao, H.S., et al., 2016. Review of fundamental properties of CO_2 hydrates and CO_2 capture and separation using hydration method. Renew. Sustain. Energy Rev. 53, 1273–1302. https://doi.org/10.1016/j.rser.2015.09.076.
Makogon, Y.F., 2010. Natural gas hydrates-A promising source of energy. J. Nat. Gas Sci. Eng. 2 (1), 49–59. https://doi.org/10.1016/j.jngse.2009.12.004.
Meng, S., Wang, W., Wang, Z., 2025. Key factors and interaction mechanisms affecting methane hydrate nucleation in W/O systems. Fuel 386, 134260. https://doi.org/10.1016/j.fuel.2024.134260.
Mikhienkova, E.I., Lysakov, S.V., Neverov, A.L., et al., 2022. Experimental study on the influence of nanoparticles on oil-based drilling fluid properties. J. Petrol. Sci. Eng. 215, 109452. https://doi.org/10.1016/j.petrol.2021.109452.
Min, J., Kang, D.W., Ahn, Y.H., et al., 2020. Recoverable magnetic nanoparticles as hydrate inhibitors. Chemical Engineering Journal 389, 124461. https://doi.org/10.1016/j.cej.2020.124461.
Natarajan, V., Bishnoi, P.R., Kalogerakis, N., 1994. Induction phenomena in gas hydrate nucleation. Chem. Eng. Sci. 49 (13), 2075–2087. https://doi.org/10.1016/0009-2509(94)E0026-M.
Ndlovu, P., Babaee, S., Naidoo, P., et al., 2024. Kinetic studies of gas hydrates for CO_2 capture in the presence of nanoparticles. Ind. Eng. Chem. Res. 63 (9), 3867–3879. https://doi.org/10.1021/acs.iecr.3c04061.s001.
Ning, F.L., Zhang, L., Jiang, G.S., et al., 2011. Comparison and application of different empirical correlations for estimating the hydrate safety margin of oil-based drilling fluids containing ethylene glycol. J. Nat. Gas Chem. 20 (1), 25–33. https://doi.org/10.1016/s1003-9953(10)60161-2.
Ning, F.L., Guo, D.D., Din, U.S., et al., 2022. The kinetic effects of hydrate anti-agglomerants. Fuel 318, 123566. https://doi.org/10.1016/j.fuel.2022.123566.
Ortiz, D.G., Pochat-Bohatier, C., Cambedouzou, J., et al., 2020. Current trends in Pickering emulsions: particle morphology and applications. Engineering 6 (4), 468–482. https://doi.org/10.1016/J.ENG.2019.08.017.
Park, J.H., Park, J., Lee, J.W., et al., 2023. Progress in CO_2 hydrate formation and feasibility analysis for cold thermal energy harvesting application. Renew. Sustain. Energy Rev. 187, 113783. https://doi.org/10.1016/j.rser.2023.113783.
Park, K.N., Sang, Y.H., Jin, W.L., et al., 2011. A new apparatus for seawater desalination by gas hydrate process and removal characteristics of dissolved minerals (Na^+, Mg^{2+}, Ca^{2+}, K^+, B^{3+}). Desalination 274 (1), 91–96. https://doi.org/10.1016/j.desal.2011.01.084.
Park, S.S., An, E.J., Lee, S.B., et al., 2012. Characteristics of methane hydrate formation in carbon nanofluids. J. Ind. Eng. Chem. 18 (1), 443–448. https://doi.org/10.1016/j.jiec.2011.11.045.
Raman, A.Y., Venkataramani, D., Bhagwat, S., et al., 2016. Emulsion stability of surfactant and solid stabilized water-in-oil emulsions after hydrate formation and dissociation. Colloids Surf. A Physicochem. Eng. Asp. 506, 607–621. https://doi.org/10.1016/J.COLSURFA.2016.06.042.
Seo, S.D., Truong-Lam, H.S., Jeon, C., et al., 2024. Simultaneous removal of multi-nuclide (Sr^{2+}, Co^{2+}, Cs^+, and I^-) from aquatic environments using a hydrate-based water purification process. J. Hazard Mater. 462, 132700. https://doi.org/10.1016/j.jhazmat.2023.132700.
Sloan, E.D., 2003. Fundamental principles and applications of natural gas hydrates. Nature 426 (6964), 353–363. https://doi.org/10.1038/nature02135.
Sloan, E.D., Koh, C.A., 2008. Clathrate Hydrates of Natural Gases, third ed. CRC Press, Boca Raton, FL. https://doi.org/10.1201/9781420008494.
Smith, R.H., Johns, E.M., Goni, G.J., et al., 2014. Oceanographic conditions in the gulf of Mexico in july 2010, during the deepwater horizon oil spill. Cont. Shelf Res. 77, 118–131. https://doi.org/10.1016/j.csr.2013.12.009.
Song, R., Yan, Y., Shang, L., et al., 2020. A comparison of kinetics and thermodynamics of methane hydrate formation & dissociation in surfactant and solid dispersed emulsion. Colloids Surf. A Physicochem. Eng. Asp. 599, 124935. https://doi.org/10.1016/j.colsurfa.2020.124935.
Talatori, S., Barth, T., 2011. Rate of hydrate formation in crude oil/gas/water emulsions with different water cuts. J. Petrol. Sci. Eng. 80 (1), 32–40. https://doi.org/10.1016/j.petrol.2011.10.010.
Veluswamy, H.P., Kumar, A., Kumar, R., et al., 2017. An innovative approach to enhance methane hydrate formation kinetics with leucine for energy storage application. Appl. Energy 188, 190–199. https://doi.org/10.1016/j.apenergy.2016.12.002.
Wang, R., Liu, T.L., Ning, F.L., et al., 2019. Effect of hydrophilic silica nanoparticles on hydrate formation: insight from the experimental study. J. Energy Chem. 30 (3), 98–108. https://doi.org/10.1016/j.jechem.2018.02.021.
Wang, Z.Y., Li, P.F., Tong, S.K., et al., 2023. Investigation on the reduction effect of QAs1 on the adhesion force between methane hydrate particles and wall droplets. Fuel 340, 127521. https://doi.org/10.1016/j.fuel.2023.127521.
Wei, Y., Maeda, N., 2023. Dry water as a promoter for gas hydrate formation: a review. Molecules 28 (9), 3731. https://doi.org/10.3390/molecules28093731.
Wu, J., Ma, G.H., 2016. Recent studies of Pickering emulsions: particles make the difference. Small 12 (34), 4633–4648. https://doi.org/10.1002/smll.201600877.
Zhang, J., Li, C., Shi, L., et al., 2022. The formation and aggregation of hydrate in W/O emulsion containing different compositions: a review. Chem. Eng. J. 445, 136800. https://doi.org/10.1016/j.cej.2022.136800.
Zhang, J.S., Lee, S., Lee, J.W., 2007. Kinetics of methane hydrate formation from SDS solution. Ind. Eng. Chem. Res. 46 (19), 6353–6359. https://doi.org/10.1021/ie070627r.
Zhao, H., Yang, Y., Chen, Y., et al., 2022. A review of multiple Pickering emulsions: solid stabilization, preparation, particle effect, and application. Chem. Eng. Sci. 248, 117085. https://doi.org/10.1016/j.ces.2021.117085.
Zhou, S.D., Yu, Y.S., Zhao, M., et al., 2014. Effect of graphite nanoparticles on promoting CO_2 hydrate formation. Energy Fuels 28, 4694–4698. https://doi.org/10.1021/ef5000886.